Waveform Model to Characterize Time-Domain Pulses Resulting in EMI on Static Energy Meters

Bas ten Have, *Student Member, IEEE*, Marco A. Azpúrua, *Senior Member, IEEE*, Tom Hartman, *Student Member, IEEE*, Marc Pous, *Member, IEEE*, Niek Moonen, *Member, IEEE*, Ferran Silva, *Senior Member, IEEE*, and Frank Leferink, *Fellow, IEEE*

***Abstract*—This article presents a time-domain waveform model developed to characterize pulsed, nonlinear, current waveforms resulting in electromagnetic interference on static energy meters. The waveform model is calculated by fitting the sampled waveform data into a linear piece-wise function through a process that involves applying algorithms of pulse extraction, change-point detection, and redundancy elimination. The model is applied to data from laboratory experiments that have indicated critical current waveforms resulting in electromagnetic interference problems with static meters. Afterwards, the parameters of the modeled waveforms are calculated in order to correlate them to metering errors. The most relevant parameters that are correlated to significant errors are the maximum slope, crest factor, pulse duration, and charge. The waveform model provides an accurate description of the complex nonlinear waveforms through simplified analytical expressions that reproduce the significant features of the interfering waveforms. This waveform modeling approach could be used to standardize the artificial test signals that are representative of realistic devices and scenarios.**

***Index Terms*—Electromagnetic interference (EMI), metering errors, nonlinear, static energy meters, time-domain, waveform model.**

I. Introduction

THE energy consumption of households, for billing purposes, is measured using static energy meters [1]. These meters are replacing the conventional electromechanical meters that use the Ferraris principle, and are widely deployed by utilities across Europe. Recently, experimental studies have shown major errors of diverse static meters in various test conditions, for example, in [2], harmonic disturbances showed errors of static meters outside the limits declared by the manufacturer. Conducted electromagnetic interference (EMI) problems were also reported in 2009, and were caused by photovoltaic (PV) installations and power drive systems [3]. Similar problems occurred with PV installations in Germany [4], [5], while in other cases, high interference levels generated by active infeed converters were observed [6]. These observations, possibly combined with a higher number of complaints and failures, resulted in faster publication of the CLC/TR50579 [7] technical report and IEC 61000-4-19 standard [8]. In more recent studies modern household appliances that behave nonlinearly have shown conducted EMI problems that resulted in static meter misreadings [9]. The size of this problem is enormous, because such nonlinear behaving appliances are used increasingly in electrical networks [10]. In this regard, misreadings were found due to dimmed lighting equipment of light-emitting diode and compact fluorescent lighting technology [11], [12], and a speed-controlled water pump [13], [14]. In [13], experimental errors in meter reading between -61% and +2675% were found. The critical waveforms drawn using the nonlinear appliances show impulsive currents with a high peak value and low root-mean-square (RMS) value [15]. A fast rising slope was found to be critical, and was higher than $0.1\ \mathrm{A}/\mu\mathrm{s}$, the corresponding critical rise times were between 2 and 150 μs. The existence of more household appliances and their relation to metering errors was reported in [16]. To regenerate such waveforms, an ac controlled-current load for controllable waveform parameters to quantify metering errors has been designed in [17]. In [18], it is shown that using only the 50 Hz component accurate electromagnetic compatible energy measurements in the presence of harmonic distortion can be performed.

Next to these laboratory experiments, it is of interest to survey the signals occurring at meter connection points in on-site situations. The existence of current waveforms with fast increasing slopes that occur in low-voltage (LV) customer terminals is shown in [19]. Furthermore, in the framework of the MeterEMI project [20], surveys are performed in modern LV distribution networks. Preliminary results are shown including networks with electric vehicle (EV) charging stations [21], and PV installations [22]. This resulted in a vast repository of datasets comprising on-site current waveform measurements.

However, a parametric definition of such critical waveform that enables their identification in real scenarios, remains an unsolved technical challenge, because of the inherent complexity

Manuscript received October 5, 2020; revised January 13, 2021 and February 9, 2021; accepted February 18, 2021. This project 17NRM02 MeterEMI has received funding from the EMPIR programme co-financed by the Participating States and from the European Union.s Horizon 2020 research and innovation programme. *(Corresponding author: Bas ten Have.)*

Bas ten Have, Tom Hartman, and Niek Moonen are with the University of Twente, Enschede, AE 7500, The Netherlands (e-mail: bas.tenhave@utwente.nl; tom.hartman@utwente.nl; niek.moonen@utwente.nl).

Frank Leferink is with the University of Twente, Enschede, AE 7500, The Netherlands, and also with THALES Nederland B.V., 7554 RR Hengelo, The Netherlands (e-mail: leferink@ieee.org).

Marco A. Azpúrua, Marc Pous, and Ferran Silva are with the Universitat Politècnica de Catalunya, 08034 Barcelona, Spain (e-mail: marco.azpurua@upc.edu; marc.pous@upc.edu; ferran.silva@upc.edu).

Color versions of one or more figures in this article are available at https://doi.org/10.1109/TEMC.2021.3062948.

Digital Object Identifier 10.1109/TEMC.2021.3062948

and diversity of the current waveforms found on-site. Therefore, simple time-domain analysis algorithms that assume bilevel pulses do not work. Collaterally, the absence of the referred parametric definition hinders the possibility of establishing new testing standards concerning the immunity of the static energy meter with respect to EMI problems.

To produce such a set of standardized artificial test signals is one of the goals of the MeterEMI project [20]. In this regard, this article aims at defining and validating a parametric model for the current waveforms that result in significant errors in static meter readings. This model must provide a simplified, yet accurate, mathematical description of the current waveforms, such that it is easy to standardize into test waveforms. Therefore, it is intended to reproduce the features that have been found to be highly correlated to the errors in the static meter readings. Then, the data collected in the previously performed laboratory experiments [13]–[15] are fitted into the waveform model for obtaining parametric versions of such current waveforms, and to evidence the important parameters to be used in future immunity test signals. Here, we focus only on the parameters that could be extracted from the modeled current waveform, however, it should be noted that the phase firing angle between the voltage and the current pulse has an influence on the error, as was already pinpointed in [2], [12], and [15]. Even though this is not investigated in this article because it is not a characteristic that is related to the modeled waveform, it should be noted that the static meter errors might be amplified because of the phase firing angle.

The rest of this article is organized as follows. Section II describes the waveforms that have been linked to significant errors in static meters. Section III presents the waveform modeling approach and it is followed by the analysis of the key waveform parameters that can be extracted from the model in Section IV. Section V discusses the critical waveform parameters related to static meter errors. Finally, Section VII concludes this article.

II. Waveforms Resulting in Significant Errors of Static Meters

The current waveforms resulting in errors on static meter readings do not follow the voltage and are nonlinear. These currents are resulting from a single appliance. Two examples, representative for the waveforms resulting in static meter errors as reported in [13]–[15], are shown in Fig. 1 and they will be referred to as pulse 1 and 2. In the waveforms, a clear current pulse is visible, and one period consists of one pulse as these waveforms are unsymmetrical/unipolar, e.g., there is no current pulse in the second half of the sine wave. It is also possible that the waveform has multiple pulses for a symmetrical/bipolar waveform or a superposition of multiple pulses, e.g., when using multiple appliances. Pulse 1 is supplied by the voltage of a buildings mains supply, while pulse 2 uses the voltage supplied by a four-quadrant amplifier and a line impedance stabilization network to provide a stable impedance, therefore, resulting in a larger voltage dip. The two current waveforms shown look slightly different, the pulse 1 rises to its peak value at once, Fig. 1(a), while the pulse 2 can be considered as a superposition

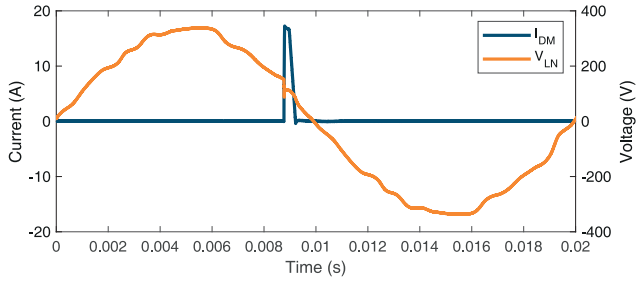

(a) Pulse 1

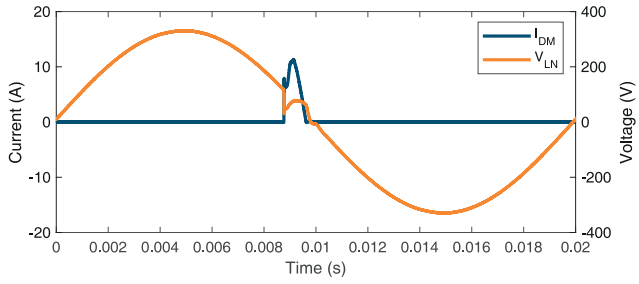

(b) Pulse 2

Fig. 1. Two different signal types considered.

of two trapezoidal pulses, it increases very fast to a first peak value around 8 A, declines, and then, it increases further to the peak value Fig. 1(b). Both pulses have a high peak value, compared to a low RMS value around 1.5 A, and therefore, a high crest factor (CF) of 10. The pulses increase very fast to their peak value, the time to rise from 10 to 90% of the pulse peak value is 20 and 3 μs for pulses 1 and 2, respectively, typical values are between 2 and 150 μs for waveforms resulting in static meter errors [15]. And the corresponding critical rising slopes are higher than 0.1 $\mathrm{A}/\mu\mathrm{s}$.

A parametric model is composed based on a set of 60 current waveforms and resulting static meter (SM) deviations during lab measurements, which were reported in [13]–[15]. The model is explained based on the waveforms presented in Fig. 1, which are representative for the set of waveforms.

III. Modeled Waveform

From the interfering pulses, a modeled waveform is composed. This modeled waveform is intended to be a simplified version of the actual current waveform while still representing all its relevant features, to make it useful for future test standards. In particular, we propose to approximate the interfering waveforms, $p(t)$, through a combination of piece-wise linear functions, $y_i(t)$, that is, a superposition of linear fitted segments given by

$$p(t) = \sum_{i=1}^{k+1} y_i(t) \tag{1}$$

where $y_i(t)$ is the equation of a straight line defined between a pair of change-points occurring at the discrete instants τ_{i-1} and

τ_i, in other words

$$y_i(t) = \begin{cases} a_i t + b_i, & \text{for } \tau_{i-1} < t \leq \tau_i \\ 0, & \text{for } t \leq \tau_{i-1} \vee t > \tau_i \end{cases}. \quad (2)$$

The piece-wise linear segments can be estimated through segmented regression if the change-points instants are known. Several computational methods for this purpose are described in [23]. Here, the underlying optimization problem is to find the optimal change-points, which means, the extreme points of each linear segment that allow an accurate representation of the measured waveform through the proposed model.

For this purpose, a three-step algorithm has been designed. First, the current pulses are extracted from the measurements, and then, they are aligned and combined for the different occurrences of the same pulse. Second, the change-point detection is implemented through the pruned exact linear time (PELT) method [24]. Third, the redundant change-points are removed to create an even more simplified representation of the interfering impulse. The details of the algorithm's steps are provided in the following subsections, and then, the waveform model is validated by comparing its fit to the original measured waveform to obtain whether this is an accurate representation.

A. Pulse Extraction

The interfering current pulse is only present in the waveform during a short time interval in each period, Fig. 1, and in the rest of the waveform, the signal has a value of zero. To analyze the pulse more thoroughly, it is extracted from the original waveform, using the process described as follows.

1) The time domain records obtained from the experiments comprise several periods of the mains frequency. The data are segmented per period (50 Hz) resulting in n frames. It might be possible that multiple pulses occur within one period, e.g., when the waveform is bipolar. In that case, the sign of the negative pulse is reversed, as a result, the frequency of pulse occurrence is doubled.
2) The peak amplitude of the pulses observed during each cycle is calculated. The interfering pulses are treated as bilevel waveforms. Consequently, the state levels are calculated according to the histogram method [25].
3) The transition instants between state levels in the rising and falling edges are detected for a mid reference level equivalent to the 10% of the difference between the high- and low-state levels. This is consistent with the commonly applied criteria of 10–90% – 90–10% used for the measurement of the rise and fall times, respectively [25].
4) The state-level tolerance, Tol, is defined considering the variation between the extremes values of the pulses' peak amplitudes according to

$$Tol\,(\%) = \pm 100 \times \frac{\max(A_{\text{peak}}) - \min(A_{\text{peak}})}{2\,\text{mean}(A_{\text{peak}})} \quad (3)$$

where the max$(\cdot)$, min$(\cdot)$, and mean$(\cdot)$ functions calculate the maximum, minimum, and average values of the pulses' peak amplitudes.

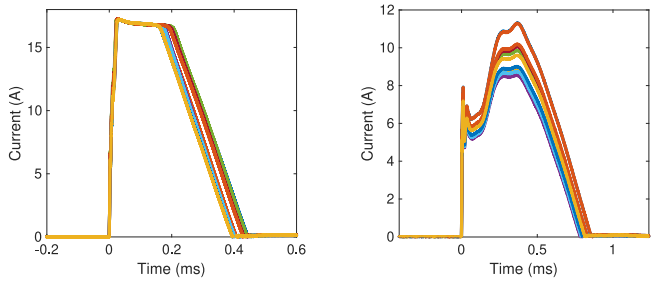

(a) Pulse 1 (b) Pulse 2

Fig. 2. Result of the pulse extraction process applied to ten cycles at mains frequency.

5) Finally, the pulses are extracted from each frame. For that purpose, the duration of the extracted waveforms is calculated as twice the maximum pulsewidth among the different pulse occurrences. The extracted pulses are then aligned with respect to the first rising edge and a time margin of 50% of the pulsewidth is allowed before and after the transition instants.

The result of the pulse extraction process is plotted in Fig. 2. Among the ten occurrences of the pulse (displayed in different colors), from pulse 2, Fig. 2(b), it is evidenced that waveform characteristics such as the peak amplitude and duration vary significantly from cycle to cycle even if the shape of the pulse remains similar.

B. Change-Points Detection

The change-point analysis is the identification of points within a dataset where certain statistical properties change. In particular, the referenced property could be the standard deviation, the RMS level, the mean value, or the slope.

Provided that each interfering pulse extracted in the previous step is represented by an ordered sequence of sampled data points $P_{1:n} = \{p_1, p_2, \ldots, p_n\}$, each point corresponding to the instants $t_{1:n} = \{t_1, t_2, \ldots, t_n\}$ and that it is of interest to fit $(t_{1:n}; P_{1:n})$ according to the model in (1) and (2) for a number of $k+1$ piece-wise linear segments, then a number of k optimal change-points, $cp_{1:k}$, must be calculated for segmenting the dataset according to abrupt changes in the waveform mean value and the slope. Those change-points occur in the discrete time instants $\tau_{1:k} = \{\tau_1, \tau_2, \ldots, \tau_k\}$. Each change-point discrete instant corresponds to a vector position that is an integer between 1 and $n-1$ inclusive.

We define $\tau_0 = t_1$ and $\tau_{k+1} = t_n$ and assume that the change-points are ordered such that $\tau_i < \tau_j$ if, and only if, $i < j$. Consequently, the k change-points will split the dataset into $k+1$ segments, with the ith segment containing $P_{(\tau_{i-1}):\tau_i}$.

One commonly used approach to identify multiple change-points is to minimize the following:

$$\sum_{i=1}^{k+1} \left[C_i\left(P_{(\tau_{i-1}):\tau_i}\right)\right] + \beta f(k) \quad (4)$$

where $C_i(\cdot)$ is the cost function for the ith segment and $\beta f(k)$ is a penalty to guard against over fitting. For linear cost functions, the PELT method is computationally efficient for finding the change-points. More about the PELT method and other algorithms for solving the previous equation is reviewed in [24].

With regards to the cost function in (4), a suitable choice is the sum of squared errors, SSE, since it is a measure of the goodness of fit that is meaningful for regression models. The SSE of the ith segment is given by

$$\mathrm{SSE}_i = \sum_{j=1}^{m} \left(p_{j,i} - y_i(t_{j,i})\right)^2 \tag{5}$$

where $(t_{j,i}; p_{j,i})$ is the time–amplitude coordinate of the jth waveform point of the ith segment containing m number of samples. A small SSE indicates a tight fit of the model to the data.

Then, the best linear fit of the subset of m waveform points in the ith segment $P_{(\tau_{i-1}):\tau_i}$ is obtained through the least squares regression, that is,

$$a_i = \frac{\sum_{j=1}^{m} \left(\bar{p}_i - p_{j,i}\right)\left(\bar{t}_i - t_{j,i}\right)}{\sum_{j=1}^{m} \left(\bar{t}_i - t_{j,i}\right)^2} \tag{6}$$

$$b_i = \bar{p}_i - a_i \bar{t}_i \tag{7}$$

where a_i and b_i are the slope coefficient and the intercept of the ith segment in (2), respectively, and $\bar{p}_i$ and $\bar{t}_i$ are the mean values of the waveform amplitudes and of their corresponding time instants, respectively.

C. Change-Points Selection

Next, the most suitable number of change-points is determined and it is decided whether or not the detected change-points are relevant to construct the model waveform. First, the appropriate number of change-points are determined. The two pulses in Fig. 1 can be described in the most simple manner by one (pulse 1) or a superposition of two pulse(s) (pulse 2). This will result in four and six change-points, for pulses 1 and 2, respectively. However, the slope of the rising part is not constant, and to retain the relevant information of the pulse, splitting (for example) the rising part in different segments allows us to retain the information about the steepest part of the slope, instead of modeling the slope as a single segment. Therefore, without making the modeled waveform too extensive, ten change-points in between the beginning and the end point of the pulse are used, so a total of twelve. The resulting modeled waveform is plotted in Fig. 3.

Second, the redundant information created by the addition of extra change-points is removed. The slopes of the consecutive linear piece-wise segments are compared and when those are similar the middle change-point is removed. It was found that when the difference between consecutive slopes is lower than 0.6% of the maximum absolute slope of the signal, the middle change-point could be removed. This simplification results in an optimized version of the model waveform that represents all the features of the original measured waveform. The redundant change-points are indicated in Fig. 3, and two and one change-points are removed for pulses 1 and 2, respectively.

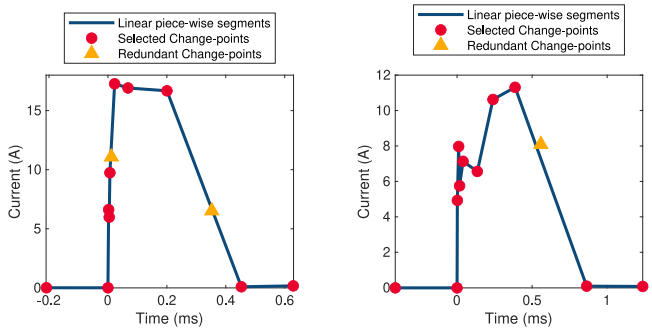

(a) Pulse 1 (b) Pulse 2

Fig. 3. Fitted modeled waveform using twelve change-points, which are either selected or provide redundant information and are removed in step 2.

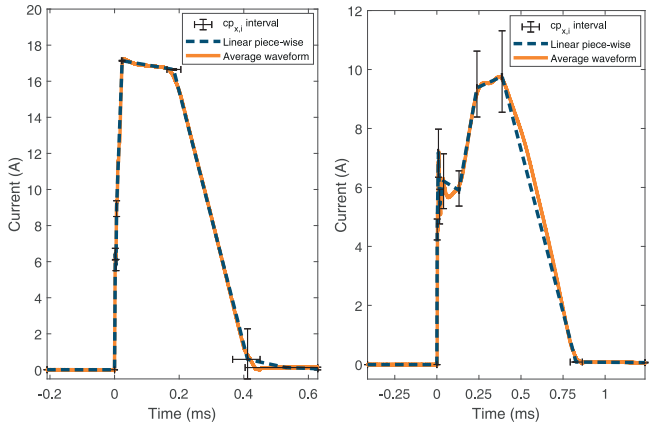

(a) Pulse 1 (b) Pulse 2

Fig. 4. Comparison between the average measured waveform and its modeled representation.

D. Modeled Waveform Validation

Validation of the model is done through comparison with the actual measured result. Fig. 4 presents a comparison between the average measured waveform and its modeled representation with each change-point indicated through its expected value and its confidence interval for the horizontal and vertical coordinates. In that sense, individual occurrences of the pulse contained between the change-points intervals are considered to be representative of the same waveform model. It is interesting to notice that the variability in the time instants of the change-points is, in general, lower than the variability in their amplitude.

As for the metric of goodness of fit, the mean squared error (MSE) between the average waveform (reference value) and the linear piece-wise model (estimated-value) was used because it provides a scalar value that is easy to calculate, compare, and interpret. For pulse 1, $\mathrm{MSE}_1 = 7.3 \times 10^{-4}$ A^2 and for pulse 2, $\mathrm{MSE}_2 = 2.8 \times 10^{-3}$ A^2. In both cases, the MSE is very low, which confirms the excellent fit observed between experimental data and the modeled waveform.

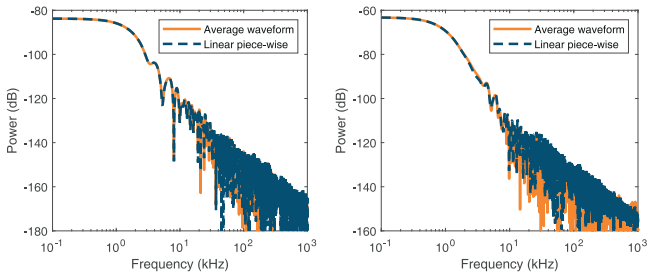

(a) Pulse 1 (b) Pulse 2

Fig. 5. Spectrum comparison between the average measured waveform and its modeled representation.

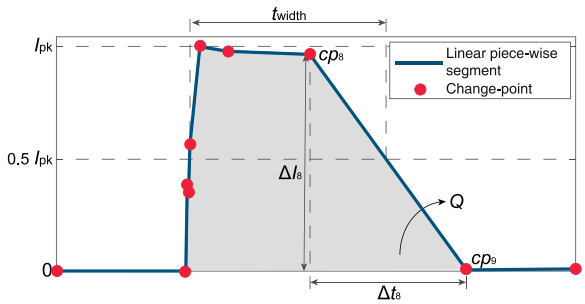

Fig. 6. Representation of the parametric description as extracted from the modeled waveform.

Likewise, the power spectrum of the measured and modeled waveforms is also in excellent agreement as is shown in Fig. 5. It evidences that no significant distortion is added to the modeled waveform and the same bandwidth is ensured. For both, pulses 1 and 2, the spectrum was calculated up to 1 MHz with a frequency resolution of 200 Hz. For this purpose, the pulse repetition frequency was the mains frequency (50 Hz), and the sampling rate used was 20 MHz.

IV. Parametric Model

In order to reduce the complexity in the description of the interfering current pulses, the modeled waveforms are characterized through a set of scalar parameters. Such that these parameters could be easily implemented in future standardized test signals. In this respect, the waveform parameters are determined for the modeled waveform, $p(t)$, and can be determined by the set $\mathbf{M}$ of k change-points, $cp_{1:k}$ as

$$\mathbf{M} = \{cp_x\{t_{x,i};\ y_i(t_{x,i})\} : x = 1, \ldots, k\}. \tag{8}$$

The extracted parameters are visualized in Fig. 6, and are explained one-by-one as follows.

1) Slope ($\Delta I/\Delta t$): The slope between two consecutive change-points, i.e., the ratio between the amplitude and time difference between consecutive change-points

$$\frac{\Delta I_x}{\Delta t_x} = \frac{y_i(t_{x+1,i}) - y_i(t_{x,i})}{t_{x+1,i} - t_{x,i}}. \tag{9}$$

A single pulse consists of multiple segments, and thus, multiple slopes. By taking the maximum or minimum value, the maximum rising or falling slope, respectively, could be determined. This is different from the commonly used 10–90% – 90–10% criteria [25], especially for the pulse 2. Where we see in Fig. 3(b) that the 90% value of the rising part is located between change-points 7 and 8, while the fastest rising part is between change-points 2 and 4. As it is expected that the fast changing edges, and thus, steep absolute slopes will contribute to misinterpretation of the measured signals in energy metering, this definition of maximum rising and falling slope is a better indication for the fast changing slopes.

2) Peak value (I_{pk}): Represents the peak value of the pulse, meaning the change-point with the highest amplitude

$$I_{\text{pk}} = \max(\{y_i(t_{x,i}) : x = 1, \ldots, k\}). \tag{10}$$

3) Pulsewidth (t_{width}): The time the signal needs in-between its rise to 50% and its fall to 50% of I_{pk}, where the time instances are interpolated on the linear piece-wise segments, this is a commonly used criteria for pulsewidth [25].

4) Charge (Q): The area circumferenced by the pulse and the zero current line; to calculate this, the area between consecutive change-points and the zero current line is determined and summed. This is a combination of a triangle with height ΔI_x and a square with height $\min(y_i(t_{x,i}), y_i(t_{x+1,i}))$, both have width Δt_x

$$Q = \sum_{x=1}^{k} \left(\frac{1}{2}\Delta I_x + \min\left(y_x(t_{x,i}), y_x(t_{x+1,i})\right) \right) \cdot \Delta t_x. \tag{11}$$

5) Crest factor (CF): The ratio between the peak value (I_{pk}) and the RMS value (I_{rms}) of the pulse over one cycle at mains frequency, this indicates how extreme the peak value of the pulse is in comparison with the rest of the signal

$$\text{CF} = \frac{I_{\text{pk}}}{I_{\text{rms}}}. \tag{12}$$

V. Critical Waveform Parameters Resulting in Metering Errors

Considering the model that accurately represents and describes the interfering current waveforms presented thus far, it is of interest to identify which, if any, of those parameters are highly correlated to the static meters errors. In order to evidence which parameters are of importance to consider in future immunity tests for EMI in static meters. However, this problem is not trivial because most parameters defined in the previous section are not independent from each other, that is, there are cross correlations and interactions between them. Additionally, the error response of the static meters to the interfering current waveforms is heterogeneous.

From the static meter data in [13]–[15], it was known that not all static meters result in the same maximum errors, as shown in Fig. 7. Therefore, the static meters are subdivided in classes, these different classes might also relate to different critical parameters. This division could also be related to the current measuring element in the static meter.

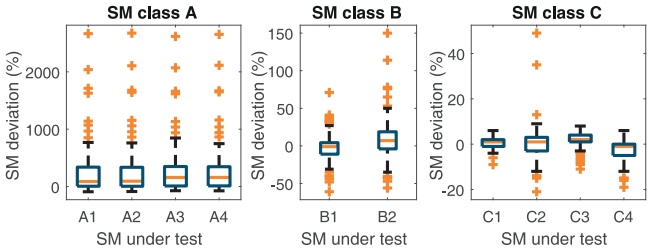

Fig. 7. Difference in the distribution of the maximum errors in static meters by class and specimen.

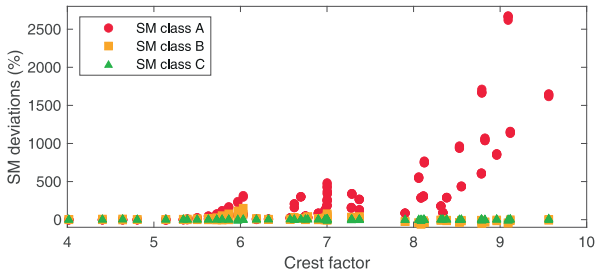

Fig. 8. Correlation between the CF and the SM deviations.

1) SM class A: Large errors, the maximum errors of the static meters above 200%; the static meters measure the current using the Rogowski coil principle.
2) SM class B: Medium errors, the maximum errors are between 50% and 200%; the static meters measure the current using the current transformer principle.
3) SM class C: Small errors, the maximum errors are smaller than 50%; the static meters measure the current using either a shunt resistor or Hall effect sensor.

In that sense, the deviations are calculated using

$$\text{SM deviation}\,[\%] = \frac{P_{\text{SM}} - P_{\text{ref}}}{P_{\text{ref}}} \cdot 100\% \qquad (13)$$

where P_{SM} is the power measured by the static meter under test and P_{ref} is the power of the reference, according to the measurement procedure explained in [13]–[15].

Now we will have a look at the correlation between the parameters and the errors for the different classes of static meters indicated, considering the meters in static meter class A. First, the correlation between the CF and static meter errors is plotted in Fig. 8, it is visible that when the CF increases the errors also increase. When the CF exceeds 5, errors start to occur. The CF provides a valuable first selector, because it already differentiates between linear and nonlinear waveforms, and will only select the pulsating waveforms. Although this correlation is clear, it is not univocal, as there are also situations where a CF higher than 5 is present, but no high error was found, so more parameters need to be considered.

Second, the correlation between the pulsewidth and the errors is plotted in Fig. 9. When the pulses become narrower than 1 ms, the static meter errors tend to increase. However, this correlation is not univocal, and within this graph, three segments are identified in which the errors increase when the pulsewidth decreases. From segment 1 to 3, the pulses peak value reduces, while the pulse contains the same range of charge. As a result, when the pulses become narrower, also the amount of charge

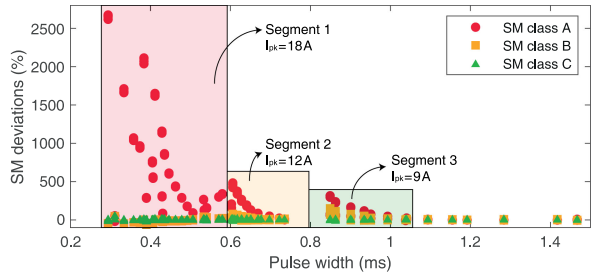

Fig. 9. Correlation between the pulsewidth and the SM deviations.

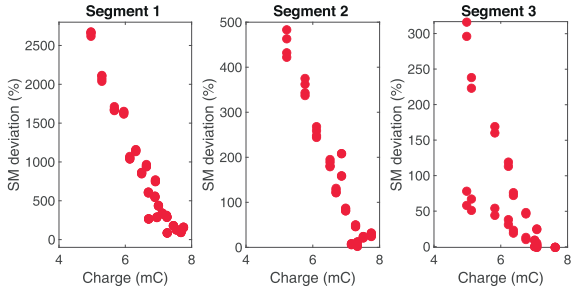

Fig. 10. Correlation between the charge and the SM deviations per segment, for SM class A.

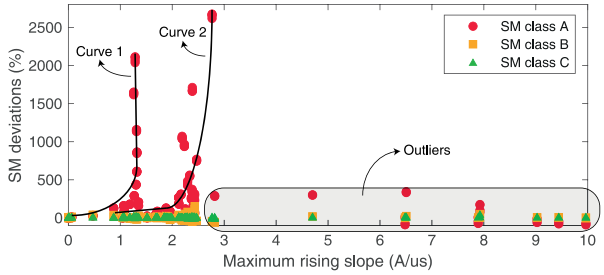

Fig. 11. Correlation between the maximum rising slope and the SM deviations.

decreases, Fig. 10, and the errors tend to increase as is visible in all three segments. It should be noted that for one static meter specimen, the errors in segment 3 increase to higher values compared to the other specimen.

Third, as already noticed, when the segments indicated before are compressed, i.e., the pulsewidth reduces from segment 1 to 2, and to 3, the peak value increases and higher errors are occurring. In that sense, higher peak values are more likely to produce higher errors, but it is more complicated than that due to interparameter dependencies.

Fourth, when the amount of charge of the pulse is decreasing, the errors tend to increase, Fig. 10 but, as we saw with the segments, the extremity of the error is then more dependent on the width of the pulse.

Fifth, the maximum slope in the rising part of the pulse is correlated to the errors in Fig. 11. In this plot, two curves are visible in which the errors increase with an increasing rising slope, and a part is visible containing outliers that do not seem to have a correlation with the maximum slope. For the outliers, the maximum slope is very large, however, the pulsewidth is really wide, in fact the pulsewidth is outside the limits of the plot in Fig. 9. The points in segments 2 and 3 are all on curve 2,

while the points in segment 1 are divided between curves 1 and 2. For the points in segment 1, the pulsewidth is really low, and the errors are more correlated to the decrease in charge rather than the slope, however, we still see an increase in errors with the slope in curves 1 and 2 for these points.

Sixth, for the maximum falling slope, so minimum slope of the pulse, no clear relationship with the errors was found, because all the pulses had similar falling slopes.

The previously noted correlations are clearly visible for SM class A in the provided plots, and they also hold for SM class B and C. In that sense, the same pulses, and thus, parameters, are resulting in errors in the static meter readings. But depending on the SM class, and thus, the current measuring element, the severity of the error is altered. However, for the meters in SM class B, the static meter errors are mostly negative when the pulses are in segment 1, and for SM class C in all segments, the errors are for the most part negative. But still the error's absolute value increases, or becomes more negative, based on the same correlated parameters discussed before.

VI. Conclusion

In this article, a parametric waveform model was shown that provided a simplified description of complex nonlinear waveforms. The identification of critical parameters had shown that erroneous waveforms are in general narrow, fast rising, pulses, where, on average, higher CF, narrower pulsewidth, higher peak amplitude, less charge, and higher slopes, will contribute to an increase in the metering error.

Furthermore, it was found that the maximum value of the static meter errors was related to the current metering element. In that sense, the Rogowski coil contributed to the highest errors, followed by the current transformer principle, and when using a shunt resistor or Hall effect sensor in most cases result in lower energy reading of the static energy meter.

In future research, the correlated parameters will be used to estimate the likelihood of errors in on-site waveforms. Likewise, this waveform modeling approach could be employed to standardize artificial test signals that are representative of the realistic devices and scenarios.

References

[1] R. Masnicki, "Some remarks on the accuracy of energy meters," in *Proc. IEEE Int. Conf. Environ. Elect. Eng./IEEE Ind. Commercial Power Syst. Eur.*, Palermo, Italy, 2018, pp. 1–5.

[2] A. Cataliotti, V. Cosentino, and S. Nuccio, "Static meters for the reactive energy in the presence of harmonics: An experimental metrological characterization," *IEEE Trans. Instrum. Meas.*, vol. 58, no. 8, pp. 2574–2579, Apr. 2009.

[3] R. B. Timens, "Electromagnetic interference of equipment in power supply networks," Ph.D. thesis, Univ. Twente, Enschede, The Netherlands, 2013.

[4] J. Kirchhof and G. Klein, "EMV - grenzwertlücke - wechselrichter stört zähler," in *Proc. 24th Symp. Photovoltaische Solarenergy*, Bad Staffelstein, Germany, 2009, pp. 1–8.

[5] J. Kirchhof, "Grenzwertlücke - wechselrichter stört elektrizitätszähler," in *Proc. Int. Trade Fair Congr. Electromagn. Compat.*, Düsseldorf, Germany, 2010, pp. 1–9.

[6] *Study Report on Electromagnetic Interference Between Electrical Equipment/Systems in the Frequency Range Below 150 kHz*, CLC/TR 50627, 2014.

[7] *Electricity Metering Equipment - Severity Levels, Immunity Requirements and Test Methods for Conducted Disturbances in the Frequency Range 2-150 kHz*, CLC/TR 50579, 2012.

[8] *Electromagnetic Compatibility (EMC) - Part 4-19: Testing and Measurement Techniques—Test for Immunity to Conducted, Differential Mode Disturbances and Signalling in the Frequency Range From 2 kHz to 150 kHz, at A.C. Power Port*, IEC 61000-4-19, 2014.

[9] F. Leferink, "Conducted interference, challenges and interference cases," *IEEE Electromagn. Compat. Mag.*, vol. 4, no. 1, pp. 78–85, Apr. 2015.

[10] M. Pourarab, S. Alishahi, and M. H. Sadeghi, "Analysis of harmonic distortion in distribution networks injected by nonlinear loads," in *Proc. 21st Int. Conf. Elect. Distrib.*, Frankfurt, Germany, 2011, pp. 6–9.

[11] F. Leferink, C. Keyer, and A. Melentjev, "Static energy meter errors caused by conducted electromagnetic interference," *IEEE Electromagn. Compat. Mag.*, vol. 5, no. 4, pp. 49–55, Oct.–Dec. 2016.

[12] Z. Marais, H. Van den Brom, G. Rietveld, R. Van Leeuwen, D. Hoogenboom, and J. Rens, "Sensitivity of static energy meter reading errors to changes in non-sinusoidal load conditions," in *Proc. Int. Symp. Electromagn. Compat.*, 2019, pp. 202–207

[13] B. ten Have, T. Hartman, N. Moonen, C. Keyer, and F. Leferink, "Faulty readings of static energy meters caused by conducted electromagnetic interference from a water pump," *Renewable Energy Power Qual. J.*, vol. 17, pp. 15–19, 2019.

[14] B. ten Have, T. Hartman, N. Moonen, and F. Leferink, "Misreadings of static energy meters due to conducted EMI caused by fast changing current," in *Proc. Joint Int. Symp. Electromagn. Compat./Asia-Pacific Int. Symp. Electromagn. Compat.*, Sapporo, Japan, 2019, pp. 445–448.

[15] B. ten Have, T. Hartman, N. Moonen, and F. Leferink, "Inclination of fast changing currents effect the readings of static energy meters," in *Proc. Int. Symp. Electromagn. Compat.*, Barcelona, Spain, 2019, pp. 208–213.

[16] R. V. Leeuwen, H. van den Brom, D. Hoogenboom, G. Kok, and G. Rietveld, "Current waveforms of household appliances for advanced meter testing," in *Proc. IEEE 10th Int. Workshop Appl. Meas. Power Syst.*, 2019, pp. 1–6.

[17] J. Dijkstra, T. Hartman, N. Moonen, and F. Leferink, "An AC controlled-current load for controllable waveform parameters to quantify static energy meter errors," in *Proc. IEEE Int. Symp. Electromagn. Compat., Signal Power Integrity*, Reno, NV, USA, 2020, pp. 472–477.

[18] T. Hartman, R. Grootjans, N. Moonen, and F. Leferink, "Electromagnetic compatible energy measurements using the orthogonality of nonfundamental power components," *IEEE Trans. Electromagn. Compat.*, early access, Sep. 18, 2020, doi: 10.1109/TEMC.2020.3019974.

[19] P. Jaques, R. Kolander, R. Hartig, R. Stiegler, A. Fröbel, and J. Meyer, "Survey of current gradient at public low voltage customer terminals in Germany," in *Proc. 25th Int. Conf. Elect. Distrib.*, Madrid, Spain, 2019, pp. 1–5.

[20] "Publishable summary for 17NRM02 MeterEMI electromagnetic interference on static electricity meters," National Physical Laboratory, Czech Metrology Institute, Justervesenet, Federal Institute Of Metrology METAS, VSL, Universitat Politècnica de Catalunya, and University of Twente, MeterEMI Tech. Rep., 2019.

[21] T. Hartman, M. Pous, M. A. Azpúrua, F. Silva, and F. Leferink, "On-site waveform characterization at static meters loaded with electrical vehicle chargers," in *Proc. Int. Symp. Electromagn. Compat.*, Barcelona, Spain, 2019, pp. 191–196.

[22] B. ten Have, M. A. Azpúrua, M. Pous, F. Silva, and F. Leferink, "On-site waveform survey in LV distribution network using a photovoltaic installation," in *Proc. Int. Symp. Electromagn. Compat.*, 2020, pp. 1–6.

[23] L. Yang, S. Liu, S. Tsoka, and L. G. Papageorgiou, "Mathematical programming for piecewise linear regression analysis," *Expert Syst. Appl.*, vol. 44, pp. 156–167, Feb. 2016.

[24] R. Killick, P. Fearnhead, and I. A. Eckley, "Optimal detection of changepoints with a linear computational cost," *J. Amer. Stat. Assoc.*, vol. 107, no. 500, pp. 1590–1598, 2012.

[25] *IEEE Standard for Transitions, Pulses, and Related Waveforms*, IEEE Standard 181-2011 (*Revision of IEEE Standard 181-2003*), pp. 1–71, 2011.

Bas ten Have (Student Member, IEEE) received the B.Sc. degree in 2015 and the M.Sc. degree in electrical engineering in 2018 from the University of Twente, Enschede, The Netherlands, where since June 2018, he has been working toward the Ph.D. degree in electromagnetic compatibility with the Power Electronics and Electromagnetic Compatibility Group.

His research interests include low-frequency electromagnetic interference, electromagnetic compatibility (EMC) in power systems, power electronics, and smart grids, energy metering, and EMC measurements.

Marco A. Azpúrua (Senior Member, IEEE) received the B.Sc. degree in telecommunications engineering and the M.Sc. degree in electrical engineering from the Universidad Central de Venezuela, Caracas, Venezuela, in 2008 and 2013, respectively, and the Ph.D. degree in electronics engineering from the Universitat Politècnica de Catalunya (UPC), Barcelona, Spain, in 2018.

He is currently a Researcher with the Electromagnetic Compatibility Group, UPC and the Co-Founder with EMC Barcelona. Previously, he was a Researcher with the Applied Electromagnetics Laboratory, Instituto de Ingeniería, Caracas. His research interests include electromagnetic compatibility, estimation of measurement uncertainty, and validation methods.

Dr. Azpúrua is a Member of the IEEE Electromagnetic Compatibility Society, the IEEE Instrumentation and Measurement Society, and the International Committee on Electromagnetic Safety. He was the recipient of the IEEE I&M Society Faculty Course Development Award in 2020 and the Best Symposium Student Paper Award at the EMC Europe International Symposium on Electromagnetic Compatibility in 2017.

Tom Hartman (Student Member, IEEE) received the Bachelor's degree in electrical engineering, in 2016 from the University of Twente, Enschede, The Netherlands and the master's degree in electrical engineering, in 2018 from the Group of Telecommunication Engineering, University of Twente, where since August 2018, he has been working toward the Ph.D. degree in electromagnetic compatibility with the Power Electronics and Electromagnetic Compatibility Group.

He is working on a project on electromagnetic interference on static electricity meters, in which he works on improving the digital signal processing techniques used for multichannel time-domain electromagnetic interference measurements.

Marc Pous (Member, IEEE) received the M.Sc. degree in telecommunications engineering and the Ph.D. degree in electronics engineering from Universitat Politècnica de Catalunya, Barcelona, Spain, in 2009 and 2015, respectively.

From 2003 to 2006, he was with the Department of Electromagnetic Compatibility, LGAI Technological Centre, Barcelona, Spain. In 2006, he joined the Electromagnetic Compatibility Group, Universitat Politècnica de Catalunya, where he is still conducting his research. He is also the Co-Founder of EMC Barcelona startup being the Business Manager of the company. He has been participating in international and national research projects related to the automotive, aerospace, railway, and medical industries. His research interest includes the development of novel time-domain interference measurement techniques and new evaluation methods to overcome not properly measured disturbances following the harmonized electromagnetic compatibility standards.

Dr. Pous is a Member of the international steering committee (ISC) EMC Europe, the Vice-Chairman of EMC Europe 2019, Barcelona, and the Treasurer of the IEEE Electromagnetic Compatibility Society Spanish chapter.

Niek Moonen (Member, IEEE) received the B.Sc. degree in advanced technology, the M.Sc. degree in electrical engineering, and the Ph.D. (*Cum Laude*) degree in electromagnetic compatibility from the University of Twente, Enschede, The Netherlands, in 2012, 2014, and 2019, respectively.

Since January 2019 he is working as a Researcher at the Power Electronics and Electromagnetic Compatibility group at the University of Twente. His research interests include electromagnetic interference (EMI) mitigation in power electronics with special interest in EMI propagation in smart grids, digital signal processing in electromagnetic compatibility measurements, and EMI filter optimization.

Dr. Moonen is a Member of the IEEE Electromagnetic Compatibility Society TC7 on low-frequency EMC and a Board Member of the Dutch EMC-ESD association.

Ferran Silva (Senior Member, IEEE) received the M.Sc. and Ph.D. degrees in telecommunications engineering from the Universitat Politècnica de Catalunya (UPC), Barcelona, Spain, in 1989 and 1997, respectively.

He is currently an Associate Professor in electronics with the Department of Electronic Engineering, UPC. Since 1993, he has been the Head with the Electromagnetic Compatibility Group, UPC (GCEM-UPC). He is the author of more than 140 publications about EMC in journals, conferences, and books. His research interests include electromagnetic compatibility (EMC) in near field and time domain, with application to transport, medical, and industrial areas. Since 1993, he has participated in 32 research projects related to EMC.

Dr. Silva is a Senior Member of the IEEE EMC Society and has been the Head of the Spanish chapter of the same society in two different periods. He is also a Member of the EMC Spanish Standardisation Committees SCTC77-210 and the CTN208 SCCISPR210 A. He was the Chairman of the EMC Europe International Symposium editions in Barcelona, in 2006 and 2019. Since 2004, he has been a Member of the EMC Europe International Steering Committee.

Frank Leferink (Fellow, IEEE) received the B.Sc., M.Sc., and Ph.D. degrees in electrical engineering from the University of Twente, Enschede, The Netherlands, in 1984, 1992, and 2001, respectively.

Since 1984, he has been with THALES, Hengelo, The Netherlands, and is currently with the Technical Authority EMC. He is also the Manager of the Network of Excellence on EMC, THALES Group, with more than 100 EMC engineers scattered over more than 20 units, worldwide. In 2003, he joined as (part-time, full research) a Professor and the Chair for EMC with the University of Twente, where he lectures the course on electromagnetic compatibility (EMC), and manages several research projects, with two researchers and 15 Ph.D. student researchers. He has authored and coauthored more than 300 papers published at international conferences or peer reviewed journals, and holds five patents.

Prof. Leferink is the past President of the Dutch EMC-ESD Association, the Chair of the IEEE EMC Benelux Chapter, a Member of ISC EMC Europe, the Chairman of EMC Europe 2018 (Amsterdam, The Netherlands), a Member of the Board of Directors of the IEEE EMC Society, and an Associate Editor for the IEEE TRANSACTIONS ON ELECTROMAGNETIC COMPATIBILITY and the IEEE LETTERS ON ELECTROMAGNETIC COMPATIBILITY PRACTICE AND APPLICATIONS.